

X-ray-scattering analysis of surface structures produced by vapor-phase epitaxy of GaAs

F. J. Lamelas* and P. H. Fuoss

AT&T Bell Laboratories, 600 Mountain Avenue, Murray Hill, New Jersey 07974

D. W. Kisker and G. B. Stephenson

IBM Research Division, Yorktown Heights, New York 10598

P. Imperatori

*Consiglio Nazionale delle Ricerche-Istituto di Teoria e Struttura Elettronica,
00016 Monterotondo Stazione, Rome, Italy*

S. Brennan

Stanford Synchrotron Radiation Laboratory, Stanford, California 94309

(Received 21 June 1993)

We have used *in situ* x-ray-scattering techniques to analyze surface reconstructions and ordered steps at various stages in the growth of GaAs by organometallic vapor-phase epitaxy. In contrast to an earlier report of a $c(4\times 4)$ reconstruction, our current measurements reveal a related structure with 1×2 symmetry. The 1×2 structure is a disordered form of the $c(4\times 4)$ reconstruction in which long-range correlations between dimer rows are preserved but dimer vacancies are located at random. Aside from reconstructions, ordered step structures were studied on samples with both high (2.2°) and low (0.07°) levels of miscut. Using Gaussian step-spacing distributions with widths of order the mean terrace size, a numerical model is used to reproduce measured truncation rod profiles in scans perpendicular to steps. We also use the model to follow the narrowing of the step-spacing distribution which occurs during growth. After the growth of several hundred angstroms of GaAs, truncation-rod profiles sharpen, accompanied by a shift in peak positions. The shift is due to an asymmetric weighting of the scattering from terraces of different widths: wide terraces make a greater contribution to the structure factor. For samples with a broadened distribution of step spacings, this effect results in a smaller peak splitting than that which would occur for an ideally miscut sample.

I. INTRODUCTION

The investigation of GaAs surface structures reported in this paper provides a close look at surfaces prepared by organometallic vapor-phase epitaxy (OMVPE). This scientifically interesting and technologically important process takes place in a physical environment which is relatively unexplored. The OMVPE process is carried out by flowing organometallic compounds [in our case trimethylgallium (TMG) and tertiarybutylarsine (TBA)] over the surface of a heated substrate. The organometallics thermally decompose at the sample surface and under suitable conditions form high-quality epitaxial films. In our experiments we apply the powerful surface x-ray scattering technique¹ to examine the in-plane surface structure (i.e., the surface reconstructions) as well as the structure along the surface normal (step structures). Although OMVPE occurs at near-atmospheric pressures, we have recently shown that highly ordered surface reconstructions^{2,3} and layer-by-layer growth⁴ occur in this chemically reactive environment.

While surface x-ray scattering techniques are applicable to a wide variety of systems, they are particularly advantageous in environments which are inaccessible to electron diffraction and microscopy. In the case at hand,

vapor-phase epitaxy takes place in flowing H_2 at a typical total pressure of 70 Torr; this precludes electron diffraction measurements. In addition, the deposition of GaAs on all heated surfaces within the reactor makes the application of tunneling or force microscopy very difficult. Aside from x-ray scattering measurements such as those discussed here, another *in situ* probe of the vapor-phase epitaxy environment which has undergone recent development is light scattering.⁵ This technique is complementary to x-ray scattering since it is sensitive to the chemical nature of the local atomic arrangements on the surface rather than the long-range surface structure.

We present the results of a study of the surface structures found on GaAs (001) immediately after layer-by-layer growth by OMVPE. In the current set of experiments we found that the surface has 1×2 symmetry and consists of a $\frac{3}{4}$ -populated excess-As dimer layer, with randomly located dimer vacancies. The random-vacancy model can be thought of as a disordered form of the $c(4\times 4)$ reconstruction reported previously in an OMVPE environment.³ In addition to the reconstructions, we have studied ordered terrace structures on these surfaces by measuring the scattering intensity in the vicinity of the 110 reciprocal-lattice position. This point lies on the 111 crystal-truncation rod which joins the 111 and $1\bar{1}\bar{1}$ bulk

diffraction peaks and it is extremely sensitive to surface roughness and the ordering of step structures. Ordered steps, which can arise during growth on crystals with a finite miscut, result in the splitting of truncation-rod profiles, due to the interference which occurs between x rays scattered from alternating terraces. In the present case we have modeled split truncation-rod profiles for samples with both small (0.07°) and large (2.2°) levels of miscut. These calculations allow us to examine the magnitude of the miscut, the statistical width of the step-spacing distribution, and the ordering of steps which occurs during layer-by-layer growth.

The data were collected during a recent two-week run at the Stanford Synchrotron Radiation Laboratory (SSRL), using a vertical axis OMVPE reactor designed for *in situ* scattering measurements.⁶ Previous GaAs growth experiments using this reactor have included studies of surface reconstructions,³ microscopic growth dynamics,⁴ and the OMVPE process in general.⁷ Measurements were performed on SSRL beamline 10-2, a 31-pole wiggler beamline with a toroidal focusing mirror, using a double-crystal Si monochromator set to provide 10 000 eV ($\lambda = 1.240 \text{ \AA}$) photons. GaAs substrates with a surface normal near [001] were attached to a Mo heating block with indium. Highly purified H_2 at a typical pressure of 70 Torr and a flow rate of 1000 standard cubic centimeters per minute (sccm) was present at all times when the samples were heated above room temperature. The organometallic compounds used in crystal growth were delivered to the substrate in parallel streams of H_2 passed through reservoirs of liquid TBA and TMG held at fixed temperatures of 20°C and -10°C , respectively. Given the comparatively high vapor pressure of As at growth temperatures greater than 500°C , a typical flow of 20 sccm through the TBA reservoir was used whenever the samples were heated above 300°C , in order to preserve an As-rich surface stoichiometry. Pulsed (10 s) GaAs growth runs were initiated by a TMG reservoir flow of 2 sccm. Under these conditions, growth is layer by layer with a rate of ~ 1 bilayer/s and an average pulse led to the deposition of ~ 12 bilayers ($\sim 35 \text{ \AA}$) of GaAs.⁴ In this paper we do not treat surface structures present *during* growth, but rather those which are present *in situ* immediately after a series of growth pulses.

In presenting the x-ray data we use bulk GaAs notation. Reciprocal-lattice axes are labeled h, k, l , with the l axis perpendicular to the sample surface. Data are plotted in reciprocal-lattice units (rlu), where $1 \text{ rlu} = 2\pi/a = 1.111 \text{ \AA}^{-1}$ and a is the GaAs lattice parameter. Given that the scattering plane and sample surface are horizontal in our setup, the in-plane ($hk0$) instrumental resolution function was defined by (i) a set of horizontal slits slightly upstream of the beamline mirror, which were set to provide low (0.5 mrad) or high (1.7 mrad) divergence $\delta(\theta)$ of the incident beam, and (ii), a set of 10 mrad Soller slits defining the 2θ resolution $\delta(2\theta)$ at a scintillation counter. These conditions produce an elongated in-plane resolution function⁸ which is tilted by $\frac{1}{2}(2\theta)$ relative to the scattering vector \mathbf{q} . The length of the resolution function is given by $k\delta(2\theta) = 0.05 \text{ \AA}^{-1} = 0.045 \text{ rlu}$, where $k = 2\pi/\lambda$. To first order, the width of

the resolution function is $q\delta\theta$, where $\delta\theta$ depends on the setting of the horizontal mirror slits and $q = \frac{4\pi}{\lambda} \sin \frac{1}{2}(2\theta)$.

II. SURFACE RECONSTRUCTION

Reconstructions were studied under a variety of conditions by performing (i) survey scans to search for reconstruction peaks and (ii) rocking scans at reconstruction positions to determine integrated intensities and transverse peak widths. Survey scans were performed on samples with the following preparation. First, GaAs was grown at temperatures ranging from 530 to 580°C . The substrates were then cooled to 300°C in a TBA flow, at which point the TBA was shut off, with the H_2 flow maintaining a pressure of 70 Torr. Survey scans were performed on several samples at 300°C in the presence of H_2 and on several samples which were cooled to less than 100°C and left in vacuum after shutting off the H_2 flow. Given that in a previous experiment³ we measured a set of intensities at $p(2\times 2)$ positions which was fully consistent with an As-rich $c(4\times 4)$ surface reconstruction, we were particularly careful to search for $c(4\times 4)$ intensities. Almost without exception the only significant intensities found during the current experiment were at 1×2 positions. During subsequent experimental runs⁹ both the $c(4\times 4)$ and 1×2 reconstructions were found during series of measurements on single samples. While the definite cause of this structural crossover has not been determined, it is most likely due to variations in substrate temperature and the partial pressures of TBA, TMG, and H_2 in the OMVPE reactor.¹⁰ In this paper we confine our analysis to the 1×2 structure.

As a typical example, we take the structure found on a sample with a miscut of less than 0.1° , corresponding to terrace widths greater than 1600 \AA , given bilayer-high steps of GaAs. The measurements discussed here were performed at 300°C in 70 Torr H_2 following the growth of $\sim 3500 \text{ \AA}$ of GaAs. A set of ω rocking curves at 21 independent 1×2 reciprocal lattice points was collected and integrated intensities were calculated by fitting the curves with a combination of Lorentzian and Gaussian functions. The number of 1×2 reflections which could be accessed is determined by a combination of the wavelength λ and the upper limit of 70° on 2θ imposed by mechanical constraints. Following correction with Lorentz and polarization factors, the integrated intensities were used to calculate the Patterson autocorrelation function,¹¹ defined as

$$P(x, y) = \sum_{hk} I_{hk0} \cos 2\pi \left(h \frac{x}{a} + k \frac{y}{a} \right), \quad (1)$$

where the sum is carried out over all measured intensities I_{hk0} and a is the GaAs lattice parameter. A contour plot¹² of the Patterson derived from the measured intensities is shown in Fig. 1. All of the peaks in the Patterson can be shown to correspond to interatomic vectors in a simple dimerization model (Fig. 2) in which atom shifts from bulk positions are confined to the upper two layers.

Given a reconstruction model such as that of Fig. 2 one can calculate scattering intensities as follows. In the kinematical approximation the structure factor is evalu-

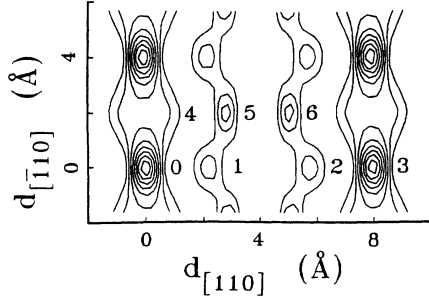


FIG. 1. Patterson (autocorrelation) function generated from measured integrated intensities at 1×2 positions. Various peaks in the Patterson function are labeled for comparison with the dimer model of Fig. 2.

ated by summing over the contribution from each atom in the sample:

$$S(\mathbf{q}) = \sum_j f_j e^{i\mathbf{q} \cdot \mathbf{r}_j} . \quad (2)$$

Here r_j is the position of the j th atom and f_j is its angle-dependent scattering factor.¹³ For surface scattering, there are two additional considerations. First, the sample is modeled as a semi-infinite bulk crystal capped by a surface reconstruction, typically one to three atomic layers thick. Second, we include the exponential penetration of x rays into the sample. The scattering factor becomes

$$S(\mathbf{q}) = \sum_{\text{bulk}} f_j e^{z_j/\tau} e^{i\mathbf{q} \cdot \mathbf{r}_j} + \sum_{\text{rec}} f_k e^{z_k/\tau} e^{i\mathbf{q} \cdot \mathbf{r}_k} , \quad (3)$$

where the two sums are over the bulk and the reconstruction, τ is the x-ray penetration depth, $z = 0$ at the terminating layer of the bulk crystal, and $z < 0$ within the bulk. Factoring both the bulk and reconstruction sums into lattice and unit cell terms we obtain

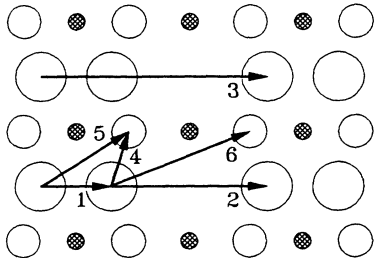


FIG. 2. The two-layer excess-As reconstruction model used in calculating scattering intensities. Arsenic atoms at the surface are shown as large open circles, those in the second layer are medium open circles, and the small shaded circles are Ga atoms which terminate the bulk crystal at the third layer from the surface. Surface As atoms form rows of dimers; the rows run vertically in this figure. Labels on vectors connecting pairs of reconstruction atoms correspond to the labels of Fig. 1. For example, vector 6 connects peaks 0 and 6 in the Patterson plot.

$$\begin{aligned} \sum_{\text{bulk}} f_j e^{z_j/\tau} e^{i\mathbf{q} \cdot \mathbf{r}_j} \\ = \sum_j e^{z_j/\tau} e^{i\mathbf{q}_z Z_j} \sum_{j'} e^{i\mathbf{q} \cdot \mathbf{R}'_j} \sum_{j''} f_{j''} e^{z_{j''}/\tau} e^{i\mathbf{q} \cdot \mathbf{r}_{j''}} , \end{aligned} \quad (4)$$

$$\sum_{\text{rec}} f_k e^{z_k/\tau} e^{i\mathbf{q} \cdot \mathbf{r}_k} = \sum_{k'} e^{i\mathbf{q} \cdot \mathbf{R}_{k'}} \sum_{k''} f_{k''} e^{z_{k''}/\tau} e^{i\mathbf{q} \cdot \mathbf{r}_{k''}} . \quad (5)$$

The unprimed sum is over columns in the bulk lattice which are perpendicular to the surface, primed sums are over the lattice projection onto the $hk0$ plane, and doubly primed sums are over individual atoms within unit cells. For reconstructed GaAs (001), the lattice is orthorhombic, with a vertical point spacing equal to the GaAs lattice parameter a and an in-plane projection (that is, the set $\{\mathbf{R}_{j'}\}$) determined by the size of the reconstruction unit cell. The sum over Z_j gives rise to the well-known crystal truncation rods:¹⁴

$$\begin{aligned} S_{\text{CTR}} &= \sum_j e^{z_j/\tau} e^{i\mathbf{q}_z Z_j} \\ &= \frac{1 - e^{i\mathbf{q}_z a} e^{-a/\tau}}{1 - 2 \cos(q_z a) e^{-a/\tau} + e^{-2a/\tau}} . \end{aligned} \quad (6)$$

For an extended surface the primed sums give rise to in-plane δ function profiles at reciprocal-lattice points with positions hk determined by the size of the reconstruction unit cell. Since we are interested in integrated intensities at fixed values of l and not the in-plane profiles of the surface peaks, we can discard the primed sums, leaving

$$S(\mathbf{q}) = \left(\frac{1 - e^{i\mathbf{q}_z a} e^{-a/\tau}}{1 - 2 \cos(q_z a) e^{-a/\tau} + e^{-2a/\tau}} \right) f_{\text{bulk}} + f_{\text{rec}} , \quad (7)$$

where f_{bulk} and f_{rec} are the doubly-primed unit-cell sums of Eqs. (4) and (5). The intensity is $I = S^* S$.

The measured integrated intensities used in generating the Patterson function of Fig. 1 are plotted in Fig. 3 along with intensities calculated using the model of Fig. 2. For simplicity, we have restricted the reconstruction to the upper two layers, which are both assigned to be As in an excess-As model. The allowed shifts in atomic positions are symmetric and horizontal (along $[110]$). There are in total four fitting parameters used in arriving at the calculated intensities of Fig. 3: horizontal shifts in the first and second As layers, an isotropic Debye-Waller factor, and an overall intensity scale factor. In addition we impose the following two constraints. First, the As-As bond lengths joining the first and second As layers are set equal to the bulk GaAs bond lengths. Thus, the horizontal dimerization is accompanied by a corresponding lowering of the top layer of atoms. This constraint has no effect at $l = 0$ (where only the projection of the

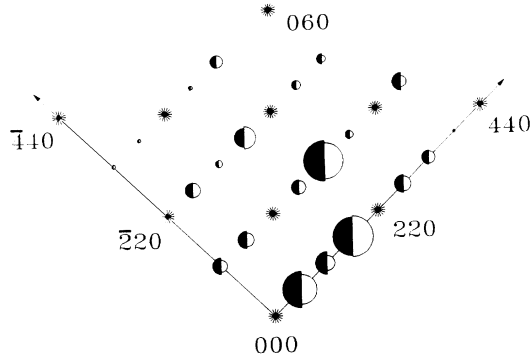


FIG. 3. Comparison of measured integrated intensities (filled semicircles) with those calculated from the model of Fig. 2, where the symbol area is proportional to the integrated scattering intensity. In the calculation the population θ_p of the upper As layer is $\frac{3}{4}$ and the horizontal As-As spacings are 2.52 Å and 3.72 Å in the first and second layers.

structure onto the $hk0$ plane contributes to the scattering intensity) and has a relatively small effect along the truncation rods. The second constraint is that the average population θ_p of the top As layer is set to 0.75 by lowering the scattering factor of the top layer by 25%. This constraint arises from the analysis of truncation rod intensities discussed below.

An optimum set of the four fitting parameters was obtained by minimizing $\chi^2 = \frac{1}{N} \sum_{j=1}^N (S_j^{\text{calc}} - S_j^{\text{meas}})^2 / \sigma_j^2$, where N is the number of measured independent reflections. For σ_j we used the *ad hoc* estimate of the error $\sigma_j = S_j^{\text{min}} + S_j^{\text{meas}}/10$, where S_j^{min} is the measured structure factor at the weakest reflection. The S_j^{min} term is used to weight the fitting towards the more intense reflections and the second term $S_j^{\text{meas}}/10$ arises from an estimated systematic error of 10% in the integrated intensities. We find that the top-layer As atoms are dimerized with a bond length of 2.52 Å and the second-layer As atoms are horizontally shifted from their bulk positions by 0.14 Å (Fig. 2). Given the bond-length constraint mentioned above, the upper-layer As atoms were lowered by 0.22 Å. The remaining parameter in our model is the Debye-Waller factor, which in our approximation is isotropic and element-independent. Multiplying the intensities by the factor $e^{-q^2 \langle \Delta x^2 \rangle}$, where $\langle \Delta x^2 \rangle$ is the projection of the mean-square atomic displacement onto the scattering vector,¹⁵ we obtain an optimum value of $\Delta x = \langle \Delta x^2 \rangle^{1/2} = 0.28$ Å.¹⁶ We note that Δx contains contributions from both thermal vibrations (here $T = 300$ °C) and static disorder. Given the dimer shifts listed above and the Debye-Waller factor, the fit to the data shown in Fig. 3 yields $\chi^2 = 0.19$ and an R factor of 14.5%, where $R = \sum |S_{\text{meas}} - S_{\text{calc}}| / \sum S_{\text{meas}}$.

Apart from determining the integrated intensities, the rocking curves through the half-order surface peaks are useful in estimating the structural correlation length L of the surface structure. There are two equivalent ways to position the dimer rows with respect to a given origin in the bulk crystal; this leads to antiphase domains in the reconstruction. The correlation length L associated with

these antiphase domains can be obtained from the reconstruction peaks by the relation $L \sim 2\pi/\delta q = 2\pi/q\delta\omega$, where $\delta\omega$ is the full width at half maximum (FWHM) of the rocking curve and q is given in Å⁻¹. After correcting for instrumental broadening due to an incident beam divergence of 1.7 mrad, the measured widths of the half-order peaks shown in Fig. 3 yield the value $\delta q = 6.6 \times 10^{-3} \pm 0.9 \times 10^{-3}$ Å⁻¹, indicating that $L \sim 1000$ Å.

Next we turn to truncation-rod intensities and the evidence for an upper As layer which is $\frac{3}{4}$ (rather than fully) populated. The effect of the population θ_p on the relative intensities at 110 and $\bar{1}10$ can be understood by reference to Fig. 2, keeping in mind that the intensity of the incident x-ray beam falls off exponentially as it enters the sample. First consider the case where there is no reconstruction and the atoms in each plane lie on a 4 Å square lattice. At the 110 diffraction condition, the scattering vector is horizontal in Fig. 2 and atoms separated by a horizontal spacing of $4n$ Å (n is an integer) scatter in phase. That is, the first layer scatters in phase with the second layer, but not with the third, and so on. For a population θ_p of the first layer, the structure factor is

$$S_{110} = \theta_p f_{\text{As}} + f_{\text{As}} t - f_{\text{Ga}} t^2 - f_{\text{As}} t^3 + f_{\text{Ga}} t^4 + f_{\text{As}} t^5 - \dots, \quad (8)$$

where t is the transmission of the x-ray beam through a single layer of GaAs. (In this approximation the transmission is equal through Ga and As layers.) Collecting terms and summing series we get

$$S_{110} = f_{\text{As}} \left(\theta_p + \frac{t}{1+t^2} \right) - f_{\text{Ga}} \left(\frac{t^2}{1+t^2} \right). \quad (9)$$

In comparison, at the $\bar{1}10$ diffraction condition the scattering vector is vertical in Fig. 2 and the second layer scatters out of phase with the first layer. In this case the structure factor is

$$S_{\bar{1}10} = \theta_p f_{\text{As}} - f_{\text{As}} t - f_{\text{Ga}} t^2 + f_{\text{As}} t^3 + f_{\text{Ga}} t^4 - \dots. \quad (10)$$

Collecting terms,

$$S_{\bar{1}10} = f_{\text{As}} \left(\theta_p - \frac{t}{1+t^2} \right) - f_{\text{Ga}} \left(\frac{t^2}{1+t^2} \right). \quad (11)$$

The ratio of the structure factors at these two points is

$$\frac{S_{110}}{S_{\bar{1}10}} = \frac{f_{\text{As}}[\theta_p(1+t^2) + t] - f_{\text{Ga}}t^2}{f_{\text{As}}[\theta_p(1+t^2) - t] - f_{\text{Ga}}t^2}. \quad (12)$$

The ratio of the intensities $I_{110}/I_{\bar{1}10}$ is given by the square of $S_{110}/S_{\bar{1}10}$. In the $t = 0$ limit only the upper monolayer is illuminated by the incident x-ray beam and as one would expect $S_{110} = S_{\bar{1}10}$. The $t = 1$ limit corresponds to an input beam grazing angle well above the critical angle for total external reflection of x rays. Using Eq. (12), we can estimate $I_{110}/I_{\bar{1}10}$ as a function of the top-layer population θ_p in this limit. For $\theta_p = 0, 0.4, 0.5, 0.75, 0.8,$ and 1.0 , we obtain $I_{110}/I_{\bar{1}10} = 1/1024,$

0.57, 1.27, 12.6, 23.9, and 1156. That is, the strong and weak scattering directions flip at $\theta_p \sim 0.5$ and $I_{110}/I_{\bar{1}10}$ reaches a maximum when θ_p is nearly 1 or a minimum when θ_p is nearly 0. In comparison, for a diamond cubic crystal such as Si the scattering factors of the two sublattices are equal and $I_{110}/I_{\bar{1}10} = 0, 1, \text{ and } \infty$ when $\theta_p = 0, 0.5, \text{ and } 1$. In general, a measurement of $I_{110}/I_{\bar{1}10}$ serves as a sensitive indication of the population of the last layer. This result is not changed drastically if the first layer is dimerized along [110] as in Fig. 2. In this case the contribution of the first layer to the structure factor S_{110} is diminished while $S_{\bar{1}10}$ is unchanged, producing a value of $I_{110}/I_{\bar{1}10}$ somewhat smaller than that predicted by Eq. (12).

While the approach given above is valid at 110 and $\bar{1}10$, we can calculate intensities along arbitrary truncation rods in the presence of surface reconstructions using Eq. (7). We have done so for $11l$ and $\bar{1}1l$ and plot these values in Fig. 4, along with measured integrated intensities. The measured ratio $I_{110}/I_{\bar{1}10}$ is close to 3, which agrees much better with a calculation using $\theta_p = \frac{3}{4}$ than with one using $\theta_p = 1$. A value of $\theta_p = \frac{3}{4}$ is consistent with the stoichiometry of the $c(4 \times 4)$ reconstruction typically found in ultrahigh vacuum.¹⁷⁻¹⁹ However, as mentioned above, careful surveys during this set of experimental runs did not reveal intensities at fractional-order reciprocal-lattice points other than 1×2 . We conclude that this surface has a stoichiometry close to that of the $c(4 \times 4)$ reconstruction, but that the dimer clusters in the upper As layer are disordered. We include the random vacancies in our calculation by multiplying the scattering factor of the upper As layer by the population θ_p .²⁰

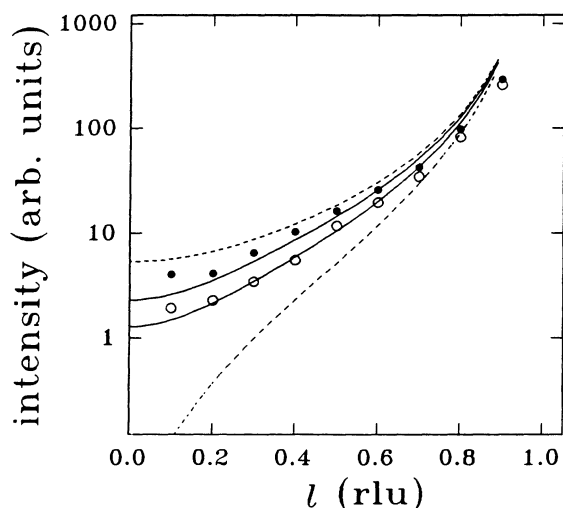


FIG. 4. Measured integrated intensities (symbols) and calculations (curves) along the $11l$ and $\bar{1}1l$ crystal truncation rods, using the model of Fig. 2. The calculation was performed using upper-As-layer populations of $\theta_p = 0.75$ (solid curves) and $\theta_p = 1.0$ (dashed curves). The filled plotting symbols and the upper two curves correspond to the $11l$ rod, while the open symbols and lower curves correspond to $\bar{1}1l$. It is clear that a fully populated upper layer of As (dashed curves) results in an intensity ratio $I_{110}/I_{\bar{1}10}$, which is too high by more than an order of magnitude.

The truncation rod data of Fig. 4 show that a reasonable value of θ_p is 0.75; this value was used in calculating the in-plane ($l = 0$) intensities of Fig. 3.

One can think of the upper layer of the $c(4 \times 4)$ reconstruction as an array of dimers with ordered vacancies, while in our 1×2 model the vacancies occur at random sites. Further evidence for such a relationship between these structures is found by comparing the measured integrated intensities at peaks which are common to both the $c(4 \times 4)$ (Ref. 3) and 1×2 reconstructions. We find that at the nine most-intense common reflections the ratio of the structure factors for the two cases is constant to within $\pm 20\%$, except at $\frac{1}{2}\frac{1}{2}0$, where the deviation from the average ratio is 30%. It is important to note that although the dimer vacancies may be disordered in the 1×2 structure, the 1000 Å correlation length derived from rocking-curve measurements at half-order peaks indicates that the dimer rows (Fig. 2) are correlated over large distances. Taken as a whole, our data are consistent with two reconstructions related by an order-disorder transformation. In the 1×2 structure, the random vacancies produce diffuse scattering intensity which collapses into the higher-order reflections of the $c(4 \times 4)$ structure as the vacancies order. To the extent that our model of the surface contains an incomplete upper As layer, it is consistent with recent calculations which indicate that complete As monolayers are unstable.²¹ Unfortunately our current measurements are rather insensitive to the admixture of Ga atoms in the second As layer suggested by recent ion-scattering measurements in ultra-high vacuum.²²

III. TERRACE STRUCTURES

Since crystal truncation rods arise from the shape transform of the sample, they are parallel to the macroscopic surface normal. In this section we discuss the analysis of truncation-rod profiles on samples for which the surface normal is not parallel to a crystalline axis. For a sample with a finite miscut, rod profiles at positions midway between two bulk reflections exhibit a splitting; each peak in the split profile arises from the truncation rod originating at one or the other of the bulk reflections. This effect is well known in both electron and x-ray diffraction and it has been treated analytically using one-dimensional models of the terrace structure²³⁻²⁵ and also in a two-dimensional Monte Carlo study.²⁶ An alternative view of the truncation-rod splitting is that it arises due to the interference between surface structures on succeeding terraces. For example, when GaAs (001) is miscut towards [110], terraces separated by bilayer steps will scatter out of phase at the 110 diffraction condition. In a scan perpendicular to the steps, this antiphase scattering causes a splitting of the truncation-rod profile into two or more satellites.

We consider several types of step-structure disorder and their effect on the truncation rod profiles.²⁷ First, step-edge roughness *per se*, on a surface where the step spacing is constant, is analogous to thermal vibration in the direction perpendicular to the step edges and leads to attenuation of higher-order peaks but no broadening in a scan perpendicular to the step edges. On the other hand,

edge roughness broadens the peaks in a scan parallel to the step edges. A second type of disorder consists of variations in step spacings. If this type of disorder is noncumulative, that is, if each step wanders about its ideal position without destroying long-range correlations, the effect is also analogous to thermal vibration and leads to the attenuation of higher-order satellites, without peak broadening either perpendicular or parallel to step edges. If the step-spacing disorder is cumulative, in the sense that a variation in the width of a given terrace shifts the positions of all succeeding terraces in the sequence, long-range correlations vanish and the rod profiles will be broadened in scans perpendicular to the step edges.

One can calculate the scattering from an arbitrary step structure by applying Eqs. (4)–(6) at each unit cell within the structure. Our approach is illustrated in Fig. 5, where we show a cross section of GaAs (001). Note that the bulk unit cell of GaAs contains four monolayers and therefore has four possible terminations. Thus the surface of a specific terrace is described by one of four possible bulk unit cells and has a corresponding surface unit cell. Denoting the height of the j th column as H_j , Eq. (4) becomes

$$S_{\text{bulk}} = \sum_{\text{bulk}} f_j e^{z_j/\tau} e^{i\mathbf{q}\cdot\mathbf{r}_j} = \left(\frac{1 - e^{iq_z a} e^{-a/\tau}}{1 - 2 \cos(q_z a) e^{-a/\tau} + e^{-2a/\tau}} \right) \times \sum_{j'} e^{i\mathbf{q}\cdot(\mathbf{R}_{j'} + H_{j'}\hat{k})} f_{\text{bulk}_{j'}}. \quad (13)$$

In contrast to the case with zero miscut discussed above, the $\mathbf{R}_{j'}$ terms can not be factored out and discarded since $f_{\text{bulk}_{j'}}$ is a function of $\mathbf{R}_{j'}$, the position of column j' in the $hk0$ plane. In a similar manner the reconstruction terms of Eq. (5) become

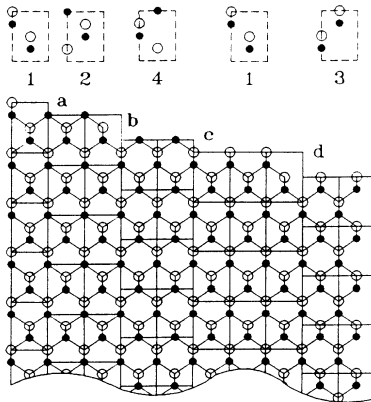


FIG. 5. Cross-sectional view of the model used in calculating scattering intensities from stepped GaAs surfaces. The crystal is factored into an array of columns; each column consists of a stack of one of four types of unit cell, depending on the termination of the column. In this example As-terminated terraces correspond to bulk unit cells labeled 1 and 3; Ga-terminated surfaces are labeled 2 and 4. Monolayer steps occur at a and c; bilayer steps are at b and d.

$$S_{\text{rec}} = \sum_{\text{rec}} f_k e^{z_k/\tau} e^{i\mathbf{q}\cdot\mathbf{r}_k} = \sum_{k'} e^{i\mathbf{q}\cdot(\mathbf{R}_{k'} + H_{k'}\hat{k})} f_{\text{rec}_{k'}}. \quad (14)$$

Note that the sums over j' and k' in Eqs. (13) and (14) are over the same surface lattice and thus they can be combined. Given the height $H_{j'}$ of each terrace, the structure factors $f_{\text{bulk}_{j'}}$ and $f_{\text{rec}_{j'}}$ are chosen from the set of four possible values by evaluating the function $\frac{a}{4}H_{j'} \bmod 4$ at each position $\mathbf{R}_{j'}$, where $a/4$ is the thickness of a single GaAs layer (see Fig. 5).

For a two-dimensional model of the surface, we create a set $\{\mathbf{R}_{j'}\}$ which describes a grid, whereas in a one-dimensional model the elements of $\{\mathbf{R}_{j'}\}$ fall on a line. In a numerical model of a disordered step structure, we start with a flat crystal and using a random-number generator we introduce steps with a Gaussian distribution of step spacings. Next we randomly insert kinks in the terrace edges with a fixed probability per edge site, subject to the constraint that step edges may not cross. This process produces a structure with a combination of edge roughness and step-spacing disorder of the cumulative type. Given a set of step-edge positions, we generate an array of $\mathbf{R}_{j'}$ and $H_{j'}$ and then evaluate Eqs. (13) and (14) at arbitrary values of the scattering vector \mathbf{q} . In a single run of the model calculation one generates a set of step positions with corresponding sharp diffraction features characteristic of that particular set. Since we wish to fit measured profiles with calculated intensities determined by a statistical distribution of structural features, we average intensities over many runs, where each run of the calculation corresponds to a unique set of step positions and edge features.

For the data discussed below, we restrict our model to bilayer (and not monolayer) steps since our samples were prepared in an As-rich environment. This is born out since the 1×2 reconstruction peaks were found only along $[110]$, and not $[\bar{1}10]$, and also by all other x-ray scattering measurements which we have made of GaAs vapor-phase epitaxy.^{3,4,7,9} Although some calculations were performed using the full two-dimensional step model (that is, including step-edge roughness), in the following we will only discuss the one-dimensional model since it produces satisfactory fits to the data in scans perpendicular to the step edges (Figs. 6–8). In order to fully explore the two-dimensional nature of the model, we would need to gather more data in scans parallel to step edges. As a further simplification, we omit surface reconstructions and include only the four bulk terminations of GaAs in the terrace structure. This restriction is not severe since we are mainly interested in individual rod profiles at $l = 0$; surface reconstruction effects would mainly consist of (i) changes in relative intensities of different truncation rods, and (ii) changes in the l dependence of truncation rod intensities. Finally, one can accelerate calculations by dividing a model structure into an array of supercells which contain integral multiples of the primitive surface cell; the creation of supercells containing n primitive cells reduces the number of terms in the structure factor by $1/n$ relative to the case where $n = 1$. This method is

acceptable as long as the size of the supercell is smaller than the size of step features which are of interest.

The measured truncation rod profile for a sample with a 0.07° miscut is shown in Fig. 6. For samples such as this one with a small miscut, the peak splitting is small and measurements were made by performing ω scans through truncation rods in order to take advantage of the superior instrumental resolution transverse to \mathbf{q} . (The horizontal slits were closed to provide an input beam divergence of 0.5 mrad for this measurement.) Given that the miscut direction is fixed in the $hk0$ plane, ω scans in different quadrants will result in different angular peak splittings and the determination of the miscut direction must be made on the basis of several rocking curve measurements.²⁴ For the sample of Fig. 6 we can unambiguously assign the miscut direction since a scan through the $13l$ rod showed no measurable splitting. Since the elongated resolution function in our setup is tilted clockwise by 13° relative to \mathbf{q} at $\bar{1}30$, the miscut direction for this sample is 5° counterclockwise from $[010]$. Given that the data in Fig. 6 were taken in a transverse scan at 110 (that is, the scan direction is along $[\bar{1}10]$), and also that the resolution function is tilted by 5.8° relative to \mathbf{q} at 110 , the measured splitting at 110 is smaller than the actual splitting by a factor of 0.77 .

The solid line in Fig. 6 is a fit to the data using the one-dimensional model described above. We used a Gaussian terrace-width distribution with a mean of 2800 Å and a FWHM of 1770 Å. The model contained 200 supercells 280 Å in size and intensities were averaged over 300 runs. The calculated profiles were convoluted with a Gaussian instrumental resolution function with a FWHM of 0.00083 Å⁻¹, determined using the width measured at a bulk GaAs reflection. For comparison, the dashed line of Fig. 6 is a calculation for a perfect terrace structure which also includes the instrumental function. (The mean terrace width for the perfect structure was

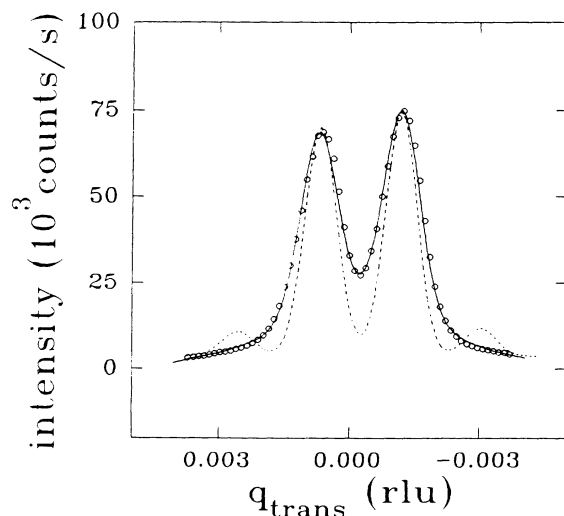


FIG. 6. Measured truncation rod profiles (symbols) and calculations (curves) at 110 , for a sample with a 0.07° miscut. In the calculation we use a mean step spacing of 2800 Å with a distribution width of 1770 Å.

3080 Å, due to the disorder-induced peak-shift effect discussed below.) The effect of the step-spacing disorder is to attenuate the second-order peaks and significantly broaden the central peaks. A similar fit to this data was obtained using a two-dimensional model with a different step-spacing distribution and significant step-edge roughness in a two-dimensional model; however, we chose to interpret the data in terms of the simpler (one-dimensional) model.

In Fig. 7 we present measured profiles for a sample with a significantly higher miscut of 2.2° along $[100]$, corresponding to much smaller 74 Å terraces. Even though the horizontal slits were opened to an input beam divergence of 1.7 mrad during these measurements, the instrumental resolution is small in comparison to the peak widths and the determination of the miscut direction is straightforward. The data consist of $[h0l]$ scans at three fixed values of l . As l increases, the left-hand peak, which is the profile of the truncation rod originating at the bulk reflection 111 , sharpens, increases in intensity, and shifts towards $h = 1$. The opposite trend occurs for the right-hand peak, which is the profile of the rod originating at $1\bar{1}\bar{1}$. The calculated profiles were obtained using a one-dimensional model with a mean step spacing of 72 Å and a step-spacing-distribution width of 60 Å. The model contained one thousand 4 -Å primitive unit cells, the out-

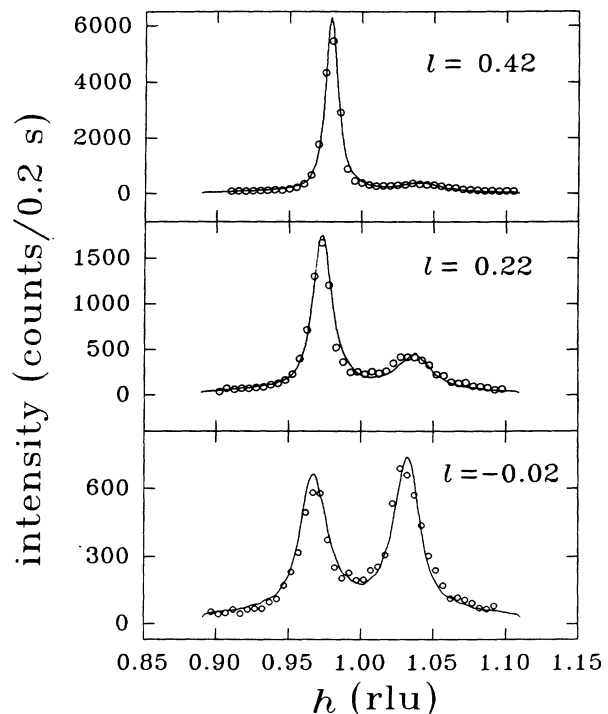


FIG. 7. Measured profiles (symbols) and calculations (curves) across the $11l$ rod, at nominal values of $l = -0.01$ (lower plot), $l = 0.19$ (center), and $l = 0.39$ (upper plot), for a sample with a 2.2° miscut along $[100]$. All calculations were performed with a mean step spacing of 72 Å and a distribution width of 60 Å. The relative scale factors used in plotting the calculated intensities were 1.0 , 0.86 , and 0.61 at $l = -0.01$, 0.19 , and 0.39 .

put was convoluted with a Gaussian instrumental function with a FWHM equal to 0.0042 \AA^{-1} , and as above the intensities were averaged over 300 runs. Two parameters were adjusted slightly from one plot to another. The first is the value of l used in the calculation, which adjusts the relative intensities of the two peaks. Whereas the data were taken at nominal values of $l = -0.01, 0.19, \text{ and } 0.39$ rlu, in the calculation we used $l = -0.02, 0.22, \text{ and } 0.42$. The second adjustable parameter is the overall intensity scale factor used in each plot, which varied from 1.00 to 0.86 to 0.61 with increasing l . These moderate adjustments in the value of l and the scale factor were made in order to correct the l dependence of the calculated truncation rod intensity; they are not surprising given that this calculation does not include surface reconstructions.

Next we turn to the evolution of terrace structure during growth. The rod profiles in Fig. 8 were taken after eight, nine, and ten GaAs growth pulses, that is, after the layer-by-layer growth of approximately 280, 315, and 350 \AA of GaAs. As growth proceeds, the measured profiles sharpen, increase in intensity, and the peak spacing increases. Given that in the simplest view the peak spacing is simply a consequence of the overall sample miscut, it is at first surprising to see this shift. For the calculated profiles of Fig. 8 we used the same model as in Fig. 7, adjusting only the width of the step-spacing distribution.

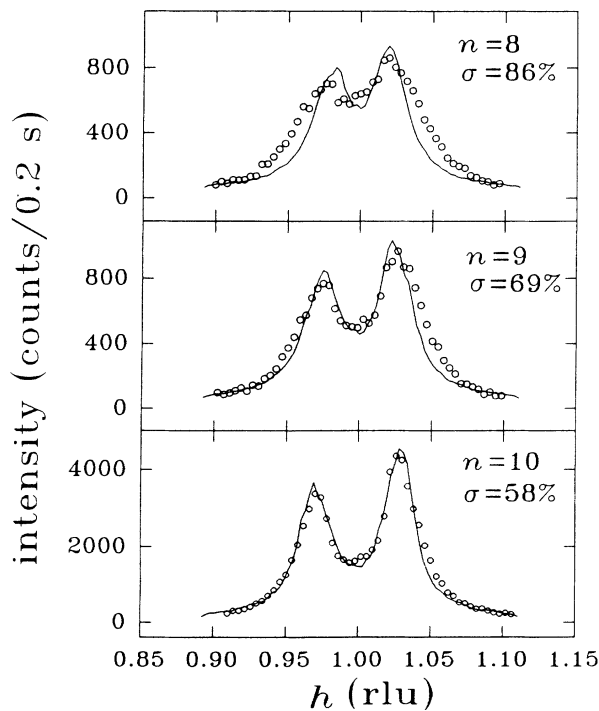


FIG. 8. Evolution of truncation-rod profiles during growth on a sample with a 2.2° miscut. The same model as in Fig. 7 was used to fit data taken after 8, 9, and 10 GaAs growth pulses. The step-spacing-distribution width was adjusted from 103 \AA to 83 \AA to 70 \AA after the growth of eight pulses (upper plot), nine pulses (center), and ten pulses (lower plot).

Although the one-dimensional Gaussian model starts to fail to reproduce the measured profile at high levels of disorder (eight growth pulses, upper plot), we can follow the evolution of the truncation-rod profiles reasonably well by simply adjusting the distribution FWHM from 103 to 83, to 70 \AA . That is, for this sample we see a pronounced ordering of the terrace structure which occurs at an overlayer thickness of several hundred \AA . Moreover, the calculations produce a peak splitting which increases with ordering, as in the measured profiles.

Given a constant nominal miscut, the actual miscut angle may shift slightly in our model for very disordered terrace structures where a non-negligible portion of the step-spacing distribution occurs at negative spacings. When negative step spacings occur during a calculation, we force the spacing to a value of one unit cell; this effect leads to a higher mean terrace spacing. Nonetheless, it is clear that the shift in the truncation-rod splitting is *not* due to changes in the macroscopic miscut angle since we see it in cases where the disorder is small enough that no negative terrace widths occur during a calculation. Moreover, the shift in peak splittings was seen in the analytical calculations of Pukite *et al.*²³ for the case of gamma distributions of step spacings with varying width, subject to the constraint that the average step spacing was preserved. We conclude that the shift arises because broader terraces (which contain more scatterers) provide a greater contribution to the structure factor than narrow terraces do. Even in a sample with a symmetric step spacing distribution, the average terrace width derived from a measurement of peak splittings will be biased towards the larger step spacings within the distribution. This effect has practical importance in the use of truncation-rod measurements to determine sample miscut: given only a measurement of the peak splitting, the calculated step spacing will only approach the actual spacing for samples with a highly ordered step structure.

IV. SUMMARY AND DISCUSSION

Overall the measurements presented above reinforce the view that surfaces in the OMVPE environment can be very highly ordered and that under suitable conditions the ordering increases following the growth of several hundred angstroms of GaAs. The surface x-ray scattering method has proven to be a very useful probe of this interesting surface ambient, and we have given detailed methods for the analysis of the x-ray data.

The 1×2 surface reconstruction which we found during this set of experiments can be thought of as a variant of the $c(4 \times 4)$ reconstruction with disordered dimer vacancies. This result is related to an earlier experiment³ where we found strong evidence for an ordered $c(4 \times 4)$ reconstruction. In a forthcoming paper⁹ we will discuss the transition between the $c(4 \times 4)$ and the 1×2 reconstructions in greater detail. Although the precise reactor conditions which stabilize the ordered vacancy structure are not yet known, it is not completely surprising that we find two related structures since there are many known surface reconstructions of GaAs (001) in ultra-high vacuum.¹⁰ It is important to note that the 1×2

structure seems to correspond to a disordering of the dimer *vacancies* of the $c(4\times 4)$ structure; the relatively narrow 1×2 rocking-curve widths indicate that the dimer rows remain ordered over a length scale of 1000 Å. Apart from our study of the reconstructions *per se*, we note the utility of the intensity ratio $I_{110}/I_{\bar{1}10}$ as a probe of the population of the last layer of the crystal.

With respect to terrace structures we find that all of our measurements in scans perpendicular to step edges can be modeled in one dimension with a Gaussian distribution of step spacings. We have shown in detail how numerical methods can be applied to the study of two-dimensional structures, and we plan to apply these methods to future measurements of truncation rod profiles parallel to step edges. Such measurements should be relatively sensitive to edge roughness, which is nearly universal in scanning tunneling microscope images of stepped surfaces. Finally, we have shown how the nar-

rowing of the step-spacing distribution during growth is accompanied by an evolution of the peak splitting in the truncation-rod profiles. For a perfectly ordered step structure the truncation-rod splitting can be used directly to measure the magnitude of the sample miscut. However, when the step-spacing distribution is broadened the measured splitting will correspond to a miscut which is smaller than the actual value.

ACKNOWLEDGMENTS

We acknowledge the considerable assistance provided by the staff of SSRL, which is supported by the Department of Energy. R. M. Lum and J. L. Kahn helped in the data collection, and I. K. Robinson discussed scattering calculations with us. One of us (F.J.L.) would like to thank Christine Orme and the Department of Physics at the University of Michigan, where he was a guest during the preparation of a portion of this manuscript.

*Present address: Department of Physics, The University of Missouri, Columbia, MO 65211.

- ¹P. H. Fuoss and S. Brennan, *Annu. Rev. Mater. Sci.* **20**, 365 (1990).
- ²D. W. Kisker, P. H. Fuoss, K. L. Tokuda, G. Renaud, S. Brennan, and J. L. Kahn, *Appl. Phys. Lett.* **56**, 2025 (1990).
- ³F. J. Lamelas, P. H. Fuoss, P. Imperatori, D. W. Kisker, G. B. Stephenson, and Sean Brennan, *Appl. Phys. Lett.* **60**, 2610 (1992).
- ⁴P. H. Fuoss, D. W. Kisker, F. J. Lamelas, G. B. Stephenson, P. Imperatori, and S. Brennan, *Phys. Rev. Lett.* **69**, 2791 (1992).
- ⁵See, for example, Itaru Kamiya, D. E. Aspnes, H. Tanaka, L. T. Florez, J. P. Harbison, and R. Bhat, *Phys. Rev. Lett.* **68**, 627 (1992).
- ⁶S. Brennan, P. H. Fuoss, J. L. Kahn, and D. W. Kisker, *Nucl. Instrum. Methods A* **291**, 86 (1990).
- ⁷D. W. Kisker, G. B. Stephenson, P. H. Fuoss, F. J. Lamelas, S. Brennan, and P. Imperatori, *J. Cryst. Growth* **124**, 1 (1992).
- ⁸The resolution function is discussed in greater detail by I. K. Robinson, in *Handbook of Synchrotron Radiation*, edited by G. Brown and D. E. Moncton (Elsevier, Amsterdam, 1991), Vol. 3.
- ⁹G. B. Stephenson, D. W. Kisker, P. H. Fuoss, A. Payne, F. J. Lamelas, and S. Brennan (unpublished).
- ¹⁰In ultrahigh vacuum the GaAs (001) surface phase diagram is particularly complex. See L. Däweritz and R. Hey, *Surf. Sci.* **236**, 15 (1990).
- ¹¹B. E. Warren, *X-ray Diffraction* (Addison-Wesley, Reading, MA, 1969).
- ¹²We plot only positive contours of the Patterson function and note that distortions are introduced by both truncation (the measurement of intensities at finite q values) and the omission of intensities at reflections coinciding with those due to the bulk. See R. Feidenhans'l, *Surf. Sci. Rep.* **10**, 105 (1989).
- ¹³We use the scattering factor expansion and coefficients given by Don T. Cromer and Joseph B. Mann, *Acta Cryst. A* **24**, 321 (1968).
- ¹⁴I. K. Robinson, *Phys. Rev. B* **33**, 3830 (1986).
- ¹⁵A. Guinier, *X-ray Diffraction* (Freeman, San Francisco, 1963).
- ¹⁶For bulk GaAs at room temperature the value $\Delta x = 0.09$ Å is given in *International Tables for X-ray Crystallography* (Kynoch, Birmingham, 1968).
- ¹⁷M. Sauvage-Simkin, R. Pinchaux, J. Massies, P. Calverie, N. Jedrecy, J. Bonnet, and I. K. Robinson, *Phys. Rev. Lett.* **62**, 563 (1989).
- ¹⁸D. K. Biegelsen, R. D. Bringans, J. E. Northrup, and L.-E. Swartz, *Phys. Rev. B* **41**, 5701 (1990).
- ¹⁹C. Deparis and J. Massies, *J. Cryst. Growth* **108**, 157 (1991).
- ²⁰See, for example, John M. Cowley, *Diffraction Physics* (North-Holland, Amsterdam, 1984).
- ²¹Takahisa Ohno, *Phys. Rev. Lett.* **70**, 631 (1993).
- ²²J. Falta, R. M. Tromp, M. Copel, G. D. Pettit, and P. D. Kirchner, *Phys. Rev. Lett.* **69**, 3068 (1992).
- ²³P. R. Pukite, C. S. Lent, and P. I. Cohen, *Surf. Sci.* **161**, 39 (1985).
- ²⁴G. Renaud, P. H. Fuoss, J. Bevk, and B. S. Freer, *Phys. Rev. B* **45**, 9192 (1992).
- ²⁵T. A. Rabideau, I. M. Tidswell, P. S. Pershan, J. Bevk, and B. S. Freer, *Appl. Phys. Lett.* **59**, 3422 (1991).
- ²⁶N. C. Bartelt, T. L. Einstein, and Ellen D. Williams, *Surf. Sci.* **244**, 149 (1991).
- ²⁷The effects of step disorder on rod profiles are discussed by M. G. Lagally, D. E. Savage, and M. C. Tringides, in *Reflection High-Energy Electron Diffraction and Reflection Electron Imaging of Surfaces*, edited by P. K. Larsen and P. J. Dobson (Plenum, New York, 1988).